The Meteoritical Society

Meteoritics & Planetary Science 58, Nr 9, 1211–1228 (2023)
doi: 10.1111/maps.14031

Metal in mesosiderites: Evidence for redox and fractional crystallization

R. G. MAYNE[1]*, L. CAVES[1], T. J. McCOY[2], R. D. ASH[3], and W. F. McDONOUGH[3]

[1]Monnig Meteorite Collection and Gallery, College of Science and Engineering, Texas Christian University, Fort Worth, Texas, USA
[2]Department of Mineral Sciences, National Museum of Natural History, Smithsonian Institution, Washington, District of Columbia, USA
[3]Department of Geology, University of Maryland, College Park, Maryland, USA
***Correspondence**
R. G. Mayne, Monnig Meteorite Collection and Gallery, College of Science and Engineering, Texas Christian University, TCU Box 298835, Fort Worth, TX 76109, USA.
Email: r.g.mayne@tcu.edu

(Received 07 July 2022; revision accepted 04 May 2023)

Abstract–Mesosiderites are an amalgamation of crustal silicates and molten metal, and their formational history is not well understood. It is widely believed that redox reactions occurred in the mesosiderites during metal–silicate mixing. Previous studies evaluated redox reactions by studying the silicates within mesosiderites, but little attention has been given to the metal for complementary evidence of such processes. Here, the evidence for redox within the metal portion of five mesosiderites is documented, most notably lower P content in the matrix metal relative to clast metal (nodule). These observations, together with the noted FeO reduction in silicates, provide further support for redox reactions occurring during metal–silicate mixing. Samples with differing Ir concentrations, such as Chaunskij and RKP A70015, have been previously classified as anomalous. However, the marked variation in highly siderophile element concentrations in all of these mesosiderites is consistent with fractional crystallization. These compositional trends could be explained by isolated metallic masses that underwent fractional crystallization before mixing or by hit-and-run collisions that produced metallic masses that ranged in size.

INTRODUCTION

Asteroidal meteorites preserve a record of the earliest stages of solar system processes. They provide us with a window into early protoplanetary formation, which include, but are not limited to the formation of condensates, collisions, accretion, disruption, thermal evolution, and differentiation. Impacts play a pivotal role in many of these processes and are invoked in the formation models of multiple meteorite groups, including mesosiderites (e.g., Scott et al., 2015 and references therein). There are a huge variety of ways in which impact processes can occur: for example, mixing material from a single body versus mixing material from different bodies.

Mesosiderites are stony iron breccias composed of almost equal amount of crustal silicates and core metal plus troilite, with the notable paucity of any mantle material. As a result, in this particular context, mesosiderites form an interesting case of mixing of crustal silicates with core metal, but in the near absence of the mantle material that might be expected if these two lithologies sample a single asteroidal body (Scott et al., 2001).

Mesosiderites are classified into three chemical/petrological subtypes (A, B, and C) based on their modal mineralogy (Hewins, 1984, 1988; Powell, 1971) and four textural subgroups (1–4) that were proposed to represent the degree of recrystallization or melting they have experienced (Floran, 1978; Hewins, 1984). Both of these classification techniques rely entirely on the characterization of only the silicate phases. The orthopyroxene abundance forms the basis of the

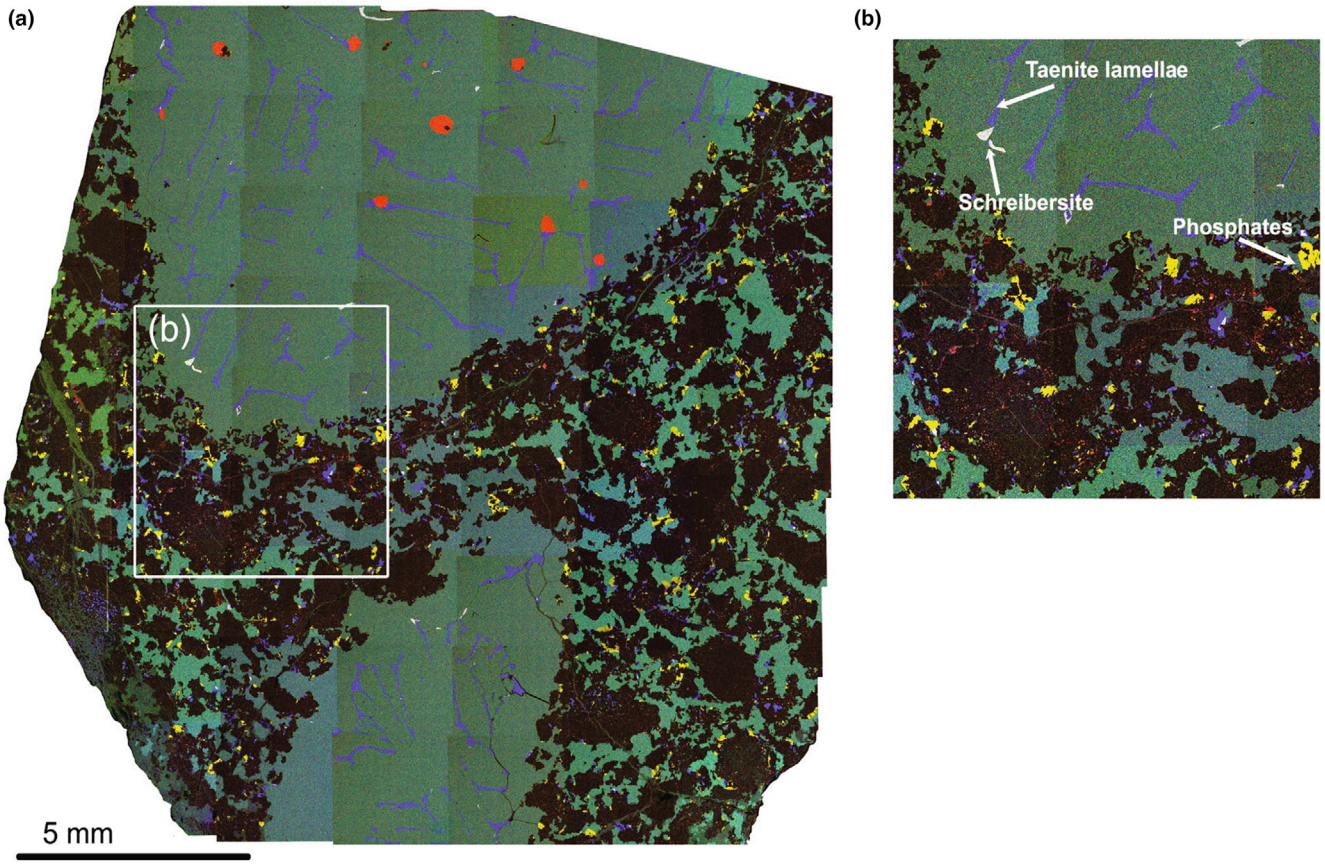

FIGURE 1. Multi-element x-ray map showing the distribution of Fe (green), Ni (blue), P (yellow), and S (red) in Crab Orchard. (a) Kamacite (green), taenite (blue), schreibersite (white), phosphate (yellow), troilite (orange) are present in this thin section. The phosphates occur in association with silicates in the matrix. Schreibersite, seen in (b) at the end of a taenite lamella, is the only P-bearing phase found in the metal clasts of Crab Orchard. Taenite rarely occurs in the matrix metal.

petrologic subtype classification as it increases in modal abundance from type A to type C. Type A mesosiderites contain mostly clinopyroxene, whereas the silicate portions within type C samples are orthopyroxenites (Hewins, 1984, 1988; Krot et al., 2014). Since it was proposed by Powell (1971), the textural classification of mesosiderites has become more complex, with multiple samples having characteristics that belong to several of the four groupings (Hewins, 1984; Krot et al., 2014). Samples are considered anomalous if they do not fit into this classification scheme.

Mesosiderite formation can be divided into three main stages: (1) Initial crystallization of mesosiderite silicates followed by a period of intense brecciation (e.g., Floran, 1978; Powell, 1971); (2) mixing of metal and silicate, resulting in local partial melting, recrystallization of silicates, and rapid cooling (e.g., Hewins, 1984, 1988; Rubin & Jerde, 1987; Scott et al., 2001; Wasson & Rubin, 1985); and (3) deep burial within their parent body, reflected by a narrow range of ^{39}Ar-^{40}Ar ages (3.7–4.1 Ga) and in the slow cooling rates of the metal (e.g., Bogard & Garrison, 1998; Bogard et al., 1990; Haack et al., 1996; Hopfe & Goldstein, 2001; Powell, 1969). This study primarily focuses on the second stage of mesosiderite formational history, where it has been proposed that redox reactions occurred between the metal and silicates during mixing (e.g., Agosto, 1985; Harlow et al., 1982; Mittlefehldt, 1990).

Mesosiderite silicates crystallized before mixing with the metal and are of crustal origin (Powell, 1971); individual grains exhibit reaction rims as a result of recrystallization (Powell, 1971). Mesosiderite silicates display a pattern of decreasing Fe/Mn and Fe/Mg, indicative of FeO reduction (Delaney et al., 1982; Mittlefehldt, 1990). The metal in mesosiderites is compositionally homogeneous compared to other iron meteorite groups and the restricted range of Ir concentrations indicates matrix metal was molten when mixing occurred (Hassanzadeh et al., 1990; Mittlefehldt et al., 1998; Powell, 1971; Wasson et al., 1974, 1998). This formational process is supported by dynamical models which indicate that impact processes are not capable of producing the level

of melting necessary to form the metal in mesosiderites (e.g., Keil et al., 1997).

While many studies have examined evidence for redox reactions during metal–silicate mixing, they have primarily focused on the silicates (e.g., Agosto, 1985; Harlow et al., 1982; Mittlefehldt, 1990). The origin of merrillite in the silicate matrix of mesosiderites has also been attributed to the oxidation of P derived from the metal (Delaney et al., 1982; Fuchs, 1969; Harlow et al., 1982; Mittlefehldt, 1990; Nehru et al., 1978; Powell, 1971). Mesosiderite metal should also preserve evidence of redox reactions if they occurred. However, there are two different populations of metal within mesosiderites: that most closely associated with the silicates (i.e., matrix metal) and metal clasts (nodules). Metal clasts present in mesosiderites were initially molten, but were solid by the time they mixed with silicate material, as indicated by the random magnetic polarity observed for the clasts within Bondoc (Nininger, 1963; Wilson, 1972) and the directional lineations observed in Bondoc and Estherville (Floran, 1978; Powell, 1971). The ellipsoidal shapes of many of the metal clasts (e.g., Crab Orchard, Figure 1) indicate that they could have been liquid droplets shaped by surface tension, as has been suggested for the metallic globules within Gujba (Rubin et al., 2003). As a result, we hypothesize that depletions in readily oxidizable elements are expected in the matrix metal relative to metal clast (nodule) material as the former was both molten during mixing and in contact with the silicates.

To assess this hypothesis, we compare the texture, metallography, mineralogy, and major, minor, and trace element composition of both the matrix and clast metal within five mesosiderites. These samples span the range of petrologic classes (A–C, anomalous) and, in order to see past the last stage of mesosiderite formation (cooling), samples that exhibit a low degree of metamorphism were chosen. They provide us with the best opportunity to assess the evidence for redox reactions within the metal portion of mesosiderites.

METHODS

We studied polished sections of four mesosiderite samples from the US National Meteorite Collection at the Smithsonian Institution's National Museum of Natural History: Crab Orchard (USNM1590), Chinguetti (USNM 3205), Chaunskij (USNM 7933), Vaca Muerta (USNM 1682), and Reckling Peak (RKP) A79015 from the U.S. Antarctic Meteorite Program, a joint venture of the Smithsonian, NASA, and NSF. These samples are characteristic of petrologic types A (Crab Orchard and Vaca Muerta), B (Chinguetti), and C (RKP A79015) and exhibit minimal metamorphism and recrystallization (subgroup 1 or 2), with the exception of Chaunskij which is highly metamorphosed and does not fit into the petrologic type classification as it contains cordierite, a silicate mineral that has not been observed in any other mesosiderite (Petaev et al., 1993; Table 1). It was included in this study due to its anomalous metal composition. Petrologic type and metamorphism subgroups are based on the silicate portion of the mesosiderites only (Floran, 1978; Hewins, 1984, 1988; Powell, 1971). While RKP A79015 is a C1 mesosiderite, it is also identified as anomalous based on the lower Ir content in its metal (Wasson et al., 1998).

TABLE 1. Classification of mesosiderites in this study, with average Fe, Ni, Co contents of electron microprobe (EMP) metal analyses[a]

	Crab Orchard (USNM1590)	Chinguetti (USNM 3205)	Chaunskij (USNM 3256)	Vaca Muerta (USNM 1682)	Reckling Peak (RKP) A79015
Petrologic type	A	B	Ungrouped, anomalous	A	C/anomalous
Metamorphic subgroup	1	1	Ungrouped, highly metamorphosed	1	2
Clast Kamacite: Fe	92.94 ± 0.91	93.15 ± 0.52	92.14 ± 0.64	94.20 ± 0.39	93.05 ± 0.43
Clast Kamacite: Ni	6.85 ± 0.20	6.33 ± 0.36	7.67 ± 0.43	5.74 ± 0.62	6.75 ± 0.18
Clast Kamacite: Co	0.73 ± 0.02	0.79 ± 0.02	0.83 ± 0.04	0.81 ± 0.02	0.79 ± 0.02
Clast Taenite: Fe	60.52 ± 0.90	61.30 ± 1.84	69.81 ± 3.83	55.18 ± 2.54	64.30 ± 3.21
Clast Taenite: Ni	38.93 ± 1.00	37.93 ± 1.85	29.69 ± 4.00	43.84 ± 2.48	34.91 ± 3.28
Clast Taenite: Co	0.28 ± 0.02	0.32 ± 0.03	0.43 ± 0.06	0.26 ± 0.01	0.37 ± 0.08
Matrix Kamacite: Fe	93.42 ± 0.62	95.16 ± 0.64	—	—	—
Matrix Kamacite: Ni	5.74 ± 0.45	5.45 ± 0.79	—	—	—
Matrix Kamacite: Co	0.17 ± 0.01	0.23 ± 0.01	—	—	—
Matrix Taenite: Fe	—	58.66 ± 4.50	—	—	—
Matrix Taenite: Ni	—	35.58 ± 17.39	—	—	—
Matrix Taenite: Co	—	below detection	—	—	—

[a]Each average is given along with its 1σ variation. All EMP analyses are provided in the supplementary information.

TABLE 2. Siderophile element abundances for Crab Orchard metal clasts collected by LA-ICP-MS.

	Re (ppm)	Os (ppm)	W (ppm)	Ir (ppm)	Mo (ppm)	Ru (ppm)	Pt (ppm)	Rh (ppm)
Kamacite	0.49	5.59	1.05	4.73	7.49	5.79	9.95	1.37
	0.50	5.68	1.03	4.91	8.06	7.20	10.01	1.27
	0.49	5.90	0.99	5.09	7.99	6.57	8.88	1.22
	0.52	5.42	0.95	4.77	7.25	4.96	8.47	1.05
	0.57	5.23	1.00	4.69	7.03	6.63	9.42	1.20
	0.47	6.22	1.26	5.12	7.13	6.48	9.63	1.09
	0.45	6.06	0.98	4.85	6.72	6.48	9.08	1.06
Average	0.50	5.73	1.04	4.88	7.38	6.30	9.35	1.18
SD	0.04	0.35	0.10	0.17	0.50	0.72	0.57	0.12
CI-norm average	12.44	11.23	11.53	10.17	7.94	9.27	9.54	8.44
Taenite	0.75	8.63	1.09	7.94	10.38	22.21	15.26	2.25
	0.89	10.52	1.26	7.93	13.7	24.38	15.62	2.26
	0.71	8.43	1.11	6.76	11.0	21.10	14.81	1.89
	0.76	9.37	1.54	7.08	11.4	20.61	15.50	1.86
	0.69	9.40	1.14	6.52	11.5	19.85	14.63	2.00
	0.87	9.32	1.09	7.89	11.9	22.13	15.46	2.27
	0.75	9.48	1.09	7.65	10.9	18.99	14.18	1.72
Average	0.77	9.30	1.19	7.39	11.55	21.33	15.06	2.03
SD	0.08	0.68	0.17	0.60	1.08	1.78	0.54	0.22
CI-norm Average	19.37	18.24	13.21	15.40	12.41	31.36	15.37	14.53

TABLE 3. Siderophile element abundances for Crab Orchard matrix metal collected by LA-ICP-MS

	Re (ppm)	Os (ppm)	W (ppm)	Ir (ppm)	Mo (ppm)	Ru (ppm)	Pt (ppm)	Rh (ppm)
Kamacite	0.51	3.25	0.67	3.56	6.49	4.72	6.84	1.03
	0.75	5.06	0.72	3.70	4.58	4.98	8.51	0.85
	0.35	4.42	0.76	3.74	3.61	5.41	8.09	0.95
	0.42	4.12	0.80	4.50	3.71	5.24	7.75	0.96
	0.43	4.81	0.78	4.13	3.00	5.21	8.03	0.87
	0.42	4.84	0.84	4.40	3.84	6.15	8.15	1.08
	0.41	5.16	1.01	4.95	3.80	6.25	9.12	0.97
	0.40	4.53	0.70	4.13	1.94	4.98	7.79	0.99
	0.47	4.43	0.66	3.83	3.03	5.09	7.89	0.88
	0.37	5.31	0.83	4.41	3.83	4.63	9.26	1.14
	0.45	4.80	0.95	4.18	3.67	5.25	8.31	0.99
	0.44	5.12	0.88	4.69	4.50	6.37	8.57	1.10
	0.48	4.90	0.95	4.61	3.50	5.78	8.96	1.14
	0.39	5.74	0.90	4.49	3.89	5.69	10.06	1.14
	0.49	4.13	0.80	3.66	3.23	4.95	8.30	1.04
	0.45	4.73	1.03	3.93	5.13	5.46	9.51	1.15
Average	0.45	4.71	0.83	4.18	3.86	5.39	8.45	1.02
SD	0.09	0.58	0.12	0.42	1.01	0.53	0.79	0.10
CI-norm average	11.31	9.23	9.22	8.71	4.15	7.92	8.62	7.27

The FEI NovaSEM 600 scanning electron microscope in the Department of Mineral Sciences at the Smithsonian Institution's National Museum of Natural History was used to produce backscattered electron images and elemental x-ray images for each polished section. Full spectrum mapping was used to produce both elemental and multi-element maps, which were used to select areas of interest for electron microprobe analysis and laser ablation-inductively coupled plasma-mass spectrometry (LA-ICP-MS) analyses.

Electron microprobe analyses were obtained using the JEOL 9800R/5 at the Smithsonian Institution's National Museum of Natural History in the Department of Mineral Sciences. Analyses included Fe, Ni, Si, S, P, Co, Cu, and Cr. Operating conditions included a fully focused beam, a current of 30 nA, and accelerating voltage energy of 20 keV. Standards used for microprobe analyses include $Ni_{10}Fe$, $Si_{3.22}Fe$, troilite (FeS), schreibersite ($[Fe,Ni]_3P$), and metallic Co, Cu, and Cr.

Minor and trace element analyses were conducted at the University of Maryland using a Thermo-Finnigan Element 2 inductively coupled plasma mass spectrometer (ICP-MS) coupled to an ultraviolet UP 213, New Wave Research laser ablation system (wavelength 213 nm).

Co (ppm)	Ni (wt%)	Fe (wt%)	Pd (ppm)	Au (ppm)	Cu (ppm)	P (ppm)	Ga (ppm)	Ge (ppm)
4999.74	6.82	92.68	3.09	0.76	73.86	—	—	—
5351.28	7.10	92.36	2.61	0.69	78.10	—	—	—
5198.95	6.96	92.52	2.86	0.91	53.10	—	10.32	58.72
4910.10	6.66	92.85	2.32	1.08	57.53	—	10.33	54.22
5161.17	6.69	92.79	2.78	0.68	76.83	409.30	—	—
4997.83	6.67	92.83	2.89	0.75	72.86	417.19	—	—
5054.72	6.46	93.03	2.46	0.96	45.40	339.75	10.72	58.56
5096	6.77	92.72	2.72	0.83	65.38	388.75	10.46	57.17
150	0.21	0.23	0.27	0.15	13.12	42.61	0.23	2.55
10.07	6.28	5.03	4.85	5.55	0.50	0.42	1.08	1.75
1132.58	38.67	61.22	18.98	3.24	1263	—	—	—
1070.94	38.34	61.55	19.03	5.90	1095	42.66	63.71	125.22
1039.62	40.84	59.06	17.07	6.12	1029	—	70.14	131.53
1080.65	39.37	60.53	16.72	5.89	1059	38.90	69.48	0.00
1116.08	38.80	61.09	17.10	3.71	1377	—	—	—
1264.63	36.35	63.53	18.42	3.41	1239	54.42	—	—
1100.03	39.36	60.53	14.70	5.14	1017	—	65.14	0.00
1114.93	38.82	61.07	17.43	4.77	1154.28	45.33	67.12	64.19
72.72	1.36	1.35	1.53	1.28	139	8.09	3.17	74.16
2.20	36.04	3.31	31.13	31.82	8.81	0.05	6.91	1.97

Co (ppm)	Ni (wt%)	Fe (wt%)	Pd (ppm)	Au (ppm)	Cu (ppm)	P (ppm)	Ga (ppm)	Ge (ppm)
4998.08	6.06	93.44	1.95	0.25	29.54	169.07	7.65	41.25
6141.77	6.24	93.07	1.90	0.40	31.90	256.32	9.20	52.70
5189.51	6.07	93.43	1.57	0.36	31.51	195.66	8.46	51.97
5459.86	5.52	93.04	2.01	0.35	20.68	128.11	9.40	60.76
4964.42	5.52	93.04	1.74	0.39	22.44	153.46	8.41	54.21
5379.26	6.29	93.36	2.00	0.39	24.99	172.89	9.36	61.62
5514.91	6.07	93.43	1.97	0.51	28.91	200.40	9.22	56.67
4791.54	4.48	94.91	1.48	0.36	15.36	116.55	8.83	51.09
4594.63	4.48	94.91	1.86	0.37	17.49	136.10	8.22	53.60
5939.06	6.24	92.42	2.51	0.53	33.34	216.16	10.78	67.20
5091.91	5.97	93.71	2.25	0.54	29.82	203.83	10.29	58.26
5263.88	6.22	92.83	2.15	0.59	31.86	202.20	10.43	60.47
5396.75	5.66	93.36	1.91	0.44	23.69	148.27	9.81	67.97
5670.86	6.28	93.12	2.60	0.51	33.41	201.18	10.52	58.98
5017.38	5.63	94.37	1.96	0.51	29.02	210.71	8.58	57.68
5180.25	5.91	93.34	2.41	0.52	29.40	196.91	9.55	53.70
5287.13	5.79	93.49	2.02	0.44	27.09	181.74	9.29	56.76
404.15	0.57	0.69	0.31	0.09	5.65	37.43	0.91	6.50
10.45	5.38	5.07	3.60	2.92	0.21	0.20	0.96	1.74

Analyses were made on both matrix metals and metal clasts for samples Crab Orchard and Chinguetti. Crab Orchard metal clasts were analyzed in two runs, the first of which produced anomalously low Ge concentrations, which we exclude from the data set presented. Metal clasts were analyzed in Chaunskij and RKP A79015. One large, segregated metal clast in Vaca Muerta was analyzed. Standard reference material used included NIST 1263a, North Chile, Coahuila, and Hoba (see Walker et al. 2008 for concentration data of standards). A normalization strategy of bulk components (Fe, Ni, Co) as 100% was employed. More information about the LA-ICP-MS specifications can be found in section A of Table S1.

RESULTS

Coordinated petrologic, major, and minor element chemical analyses allow differences in chemistry potentially related to redox reactions to be placed in the context of spatial relationships. Multi-element maps produced from combining individual elements illustrate the relationship between clasts and matrix and the mineralogy and textures in each.

Type A and B Mesosiderites

Kamacite, taenite, troilite, phosphates, and the phosphide schreibersite were identified using multi-element maps of Fe, Ni, and P. Crab Orchard (A1) matrix and clast metal were clearly distinguished in this section, metal clasts sometimes exceeded 1 cm in diameter (Figure 1). Clasts exhibit a Widmanstatten pattern with kamacite lamellae of 0.75–1 mm in width and L/W (length/width) of ~3, as observed in planar view. Minor troilite and rare schreibersite were observed; phosphates and silicates are absent, within the clasts. Silicate grains up to ~2 mm are mixed with matrix. Kamacite dominates the matrix metal grains with taenite occurring rarely and as ~100 μm grains. Matrix schreibersite is present, but phosphates are the dominant P-bearing phase.

Limited compositional variations of Fe, Ni, and Co in kamacite and taenite (Table 1, with detailed analyses given in Tables S2 and S3) demonstrate relative homogeneity within each phase, though only kamacite could be analyzed in the matrix metal. Highly and moderately siderophile elements (Re, Os, W, It, Mo, Ru, Pt, Rh, Co) are enriched at ~10 × CI for both matrix and clast metal (Tables 2 and 3; Figure 2), whereas volatile siderophiles (Cu, P, Ga, Ge) are depleted at ~0.1 to 1 × CI. As only kamacite was measured in the matrix, clast and matrix kamacite compositions are compared in Figure 2. For most highly and moderately siderophile elements, there is no significant compositional difference between matrix and clast metal, except for a pronounced depletion in Mo relative to similarly volatile elements in the matrix. Clasts, as compared to the matrix, have higher Pd, Au, Cu, and P, although P data are limited and there is some overlap between Pd and Au values between the two phases (Figure 2a). These data were double normalized to both CI and Ni-content to evaluate the relative influence of volatility versus redox between the matrix and clast metal (Figure 2b). Ni is suitable for this purpose as it condenses out of the nebula close to the temperature range of most of the condensable matter and is more strongly siderophile than Ni. The depletions in Pd, Au, Cu, and P are still present within the clast kamacite, but the Pd depletion is reduced and within error of the matrix data.

Compositional differences between kamacite and taenite within the clasts are observed (Table 2; Figure 4a). Taenite exhibits higher concentrations for most siderophile elements at ~20 to 30 × CI, exceptions are Co, Fe, and P, which are slightly to strongly depleted in taenite relative to kamacite (Figure 4a). The depletions in Co and P, as for Fe, are likely the result of the higher Ni in taenite relative to kamacite.

Compositional distinctions between clast and matrix kamacite in Chinguetti (B1) are less pronounced than for to Crab Orchard (Figure S2 vs. Figure 2; Tables S13 and S15 versus Tables 2 and 3), and no matrix metal analyses were taken for Vaca Muerta (A1). Because this work focuses primarily on the matrix and clast metal compositional difference, most data for these meteorites are included in Supplementary Material (Section E: Chinguetti; Section F: Vaca Muerta). Highly and moderately siderophile elements in Chinguetti and Vaca Muerta kamacite are enriched at ~10 × CI and volatile siderophiles depleted at ~0.1 to 1 × CI (Figure 3 and Figure S4). Overprinted on this pattern are depletions of Mo relative to surrounding elements (Ir and Ru). Although data for volatile siderophiles in kamacite and taenite are limited, both meteorites exhibit enrichments of most siderophile elements in taenite relative to kamacite with the exception of Co, Fe, and P, as also observed in Crab Orchard (Figure 4 and Figure S4).

Type C Mesosiderites

The multielement map of RKP A79015 (C-an) (Figure 5) illustrates a gradual transition from clast to matrix metal along the length of the section. In the clast, kamacite exhibits an amoeboid texture, and both schreibersite and phosphate are present. Schreibersite grains are 0.3–1 mm. Phosphate grains are ~100 μm in size and are directly associated with isolated silicate clasts within the metal clast. Matrix metal is intimately mixed with silicates and occurs in an interconnected vein network with individual veins having lengths up to ~1.75 mm. Kamacite dominates the matrix metal with rare taenite grains of ~100 μm. Phosphate grains ~100 μm in size occur sporadically throughout the matrix metal. Small schreibersite grains, ~100 μm, occur throughout the matrix but are less common. Schreibersite grains, ~0.1 to 1 mm, are also present.

Major element concentrations (Fe, Ni, Co) in kamacites show limited variation (Table 1, with detailed information given in Table S8). In contrast to A and B mesosiderites, the kamacites in type C mesosiderites have lower abundances of Re, Os, and Ir (~1 to 3 × CI) relative to the moderately siderophile elements (~3 to 5 × CI; Table 4 and Table S9; Figure 3). The volatile siderophiles exhibit depletions relative to the moderately siderophile elements and, as with types A and B mesosiderites, taenite shows higher concentrations in most siderophile elements, excluding Co, Fe, and P.

Mesosiderites with Anomalous Petrologic Type

The section of Chaunskij (an) (Figure 6) examined here consists mostly of massive metal, ~1 cm wide, and a

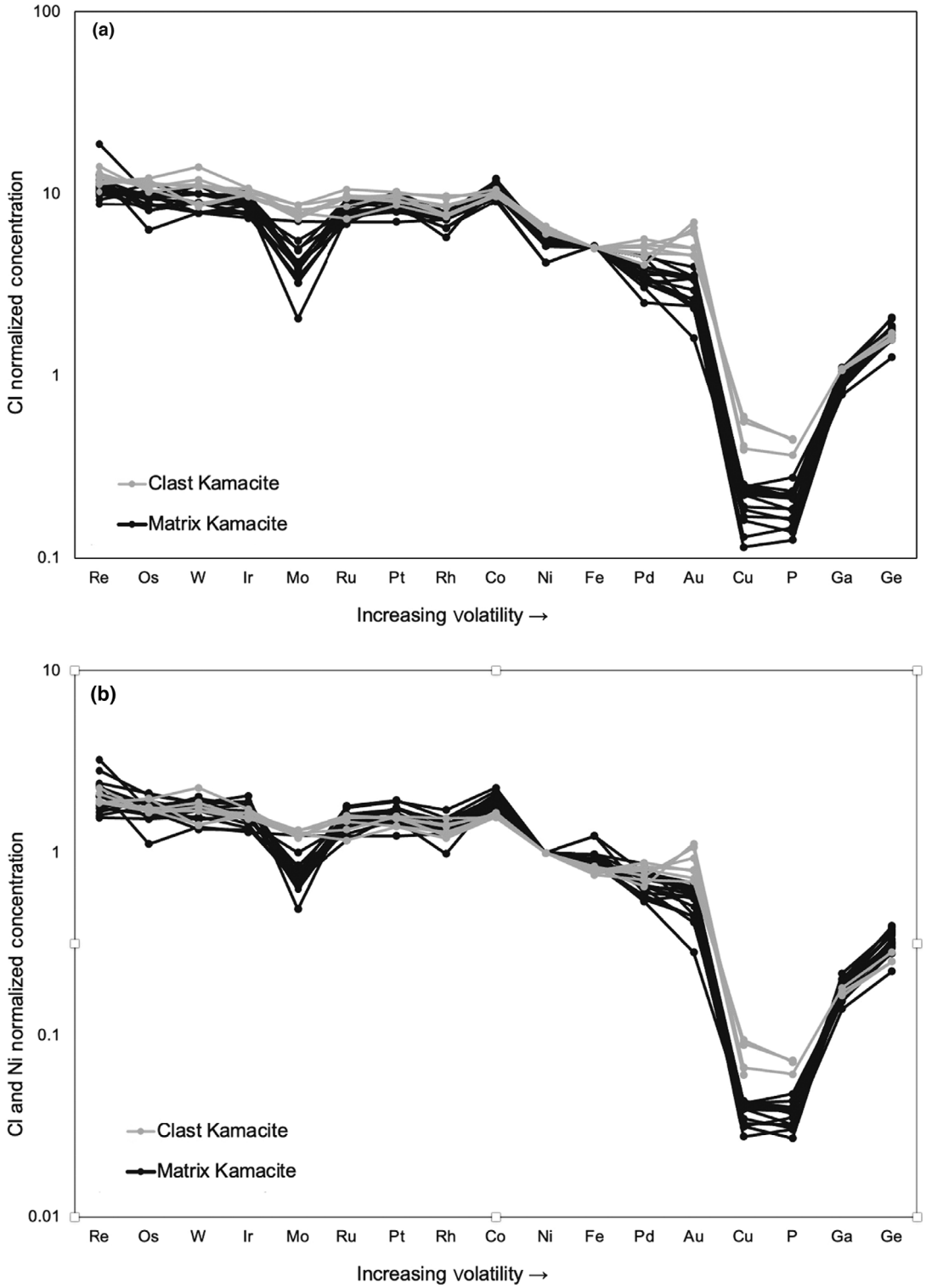

FIGURE 2. Comparison of Crab Orchard metal clast kamacite and matrix metal kamacite compositions in (a) CI normalized data (b) CI and Ni double normalized data. Clast kamacite siderophile concentrations (gray) matrix kamacite siderophile concentrations (black). Both plots shows the depletions of Mo, Cu, and P and an enrichment of Pd in the matrix kamacite compared to the metal clasts.

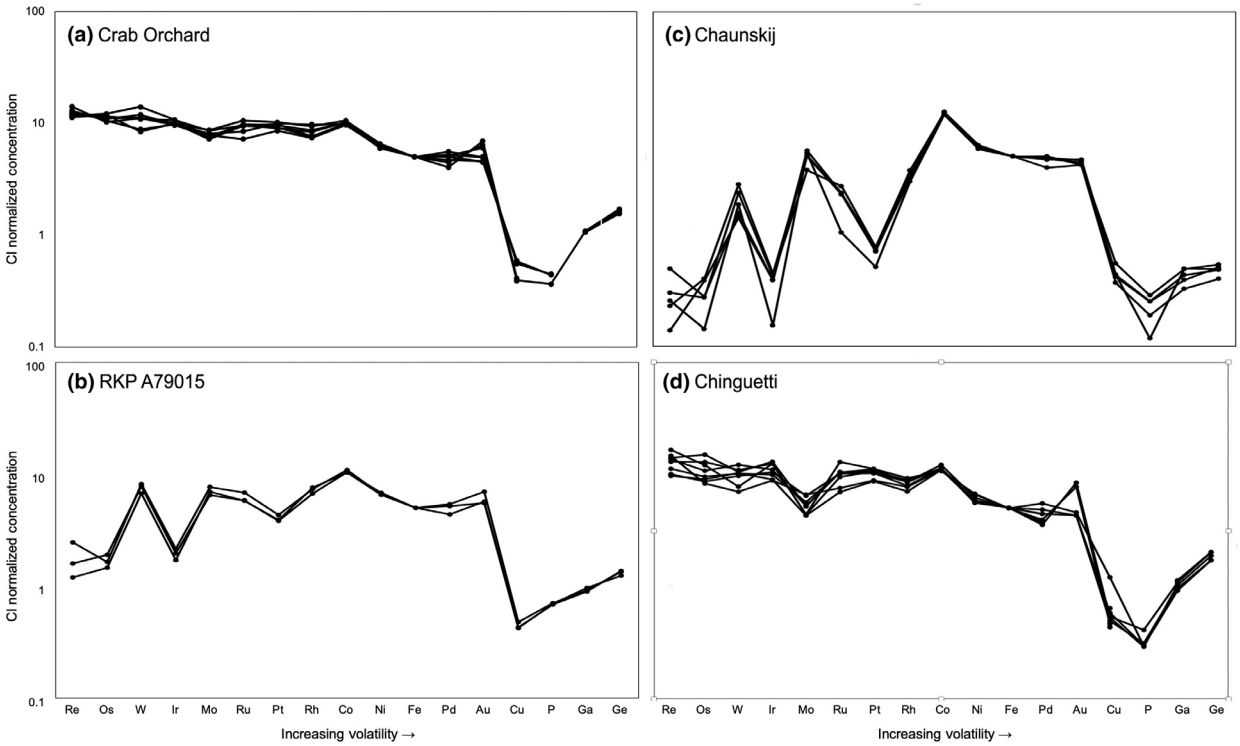

FIGURE 3. Siderophile element concentrations in clast kamacite for (a) Crab Orchard, (b) RKP A79015, (c) Chaunskij, and (d) Chinguetti.

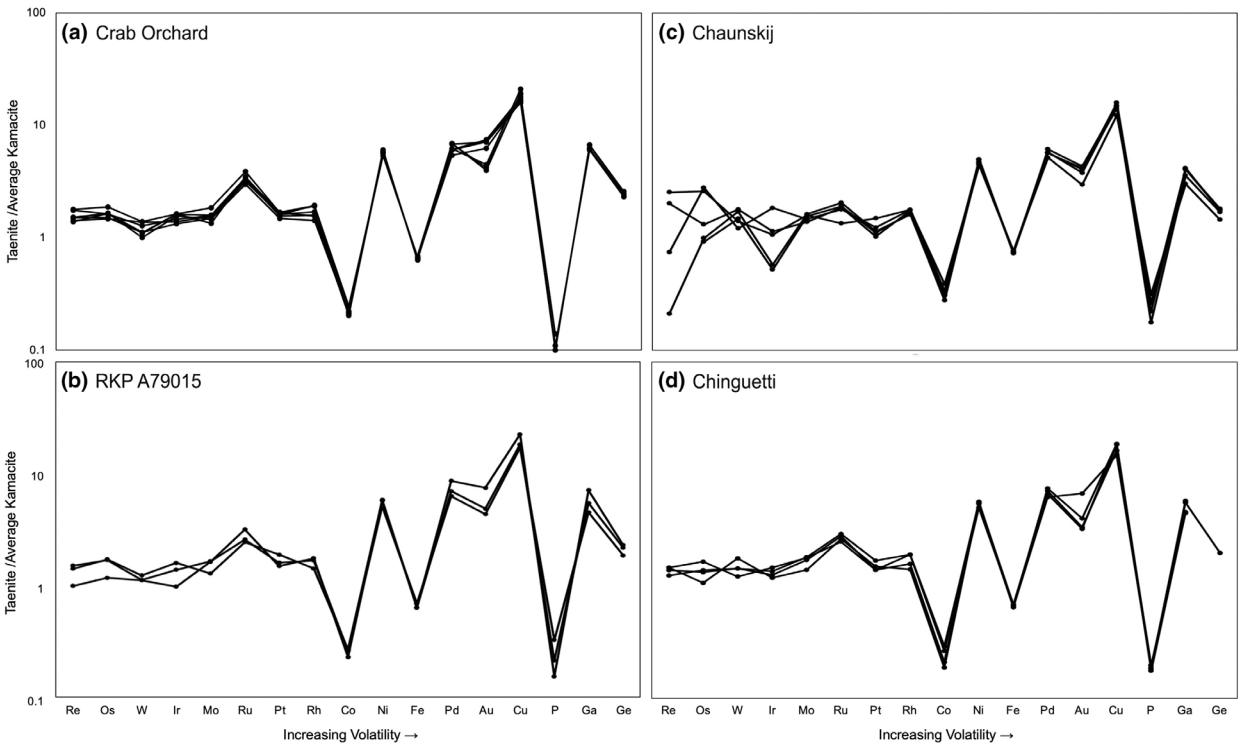

FIGURE 4. Siderophile element concentrations in clast taenite normalized to the average kamacite value for (a) Crab Orchard, (b) RKP A79015, (c) Chaunskij, and (d) Chinguetti.

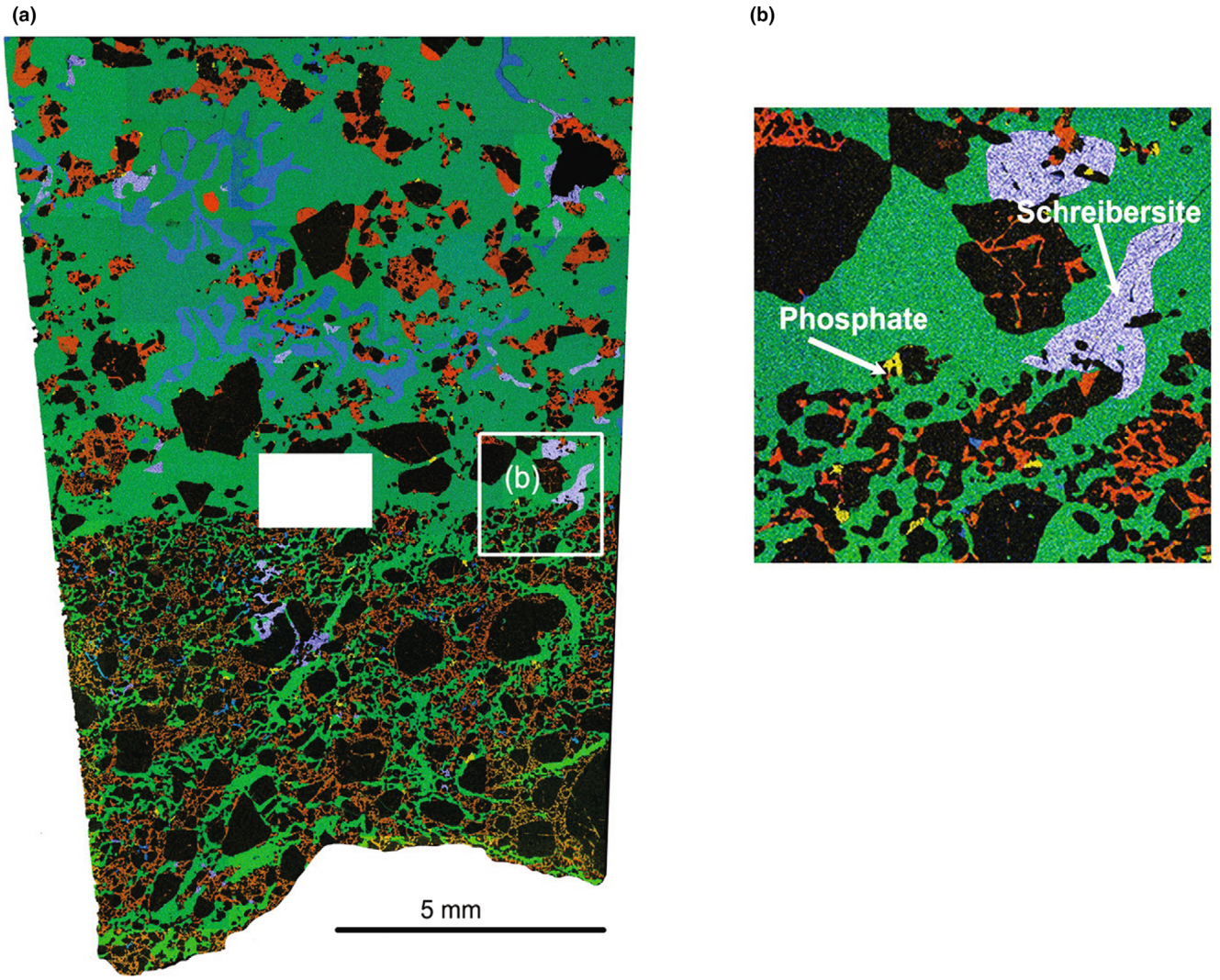

FIGURE 5. Multi-element x-ray map showing the distribution of Fe (green), Ni (blue), P (yellow), and S (red) in RKP A79015. (a) Kamacite (green), taenite (blue), schreibersite (white/lilac), phosphate (yellow), troilite (orange) are present in this sample. Metal shows a gradual transition from matrix to clast. (b) Phosphate grains are much smaller than schreibersite grains and are associated with isolated silicate clasts within the metal clast and with silicates in the matrix metal. Taenite rarely occurs in the matrix metal.

single silicate clast, ~0.5 cm × 0.5 cm. Metal is rare within the silicate clast, ranging from ~100 μm to 0.5 mm. Kamacite exists as amoeboid patches in the metal clast, and a large sinuous grain of troilite in the metal clast is ~0.4 cm long. Schreibersite grains (~0.3 mm long) exist only in the metal clast in close association with both taenite and troilite. Phosphate grains, ~0.5 to 1 mm, are in the metal clast and along the edges of the large silicate clast; smaller phosphates, ~100 μm, exist in the matrix metal.

Kamacite and taenite major element concentrations (Fe, Ni, and Co) reveal greater heterogeneity in the metal clast compared to types A, B, and C mesosiderites (Figures 3 and 4; Table 1, with detailed analyses given in Table S6). Chaunskij shows depletions in Re, Os, and Ir (~0.3 to 0.5 × CI) in comparison to the moderately siderophile elements (~10 × CI). This same pattern occurs in type C mesosiderites, but the highly siderophile element depletion in Chaunskij is of greater magnitude (Table 5 and Table S7; Figure 3c). Volatile siderophile element concentrations are depleted relative to moderately siderophiles, with similar Cu and P concentrations to types A and B mesosiderites (0.2–0.5 × CI). Much like in types A, B, and C mesosiderites, taenite shows higher concentrations of most siderophile elements, except Co, Fe, and P.

TABLE 4. Siderophile element abundances for RKP A79015 metal clast collected by LA-ICP-MS.

	Re (ppm)	Os (ppm)	W (ppm)	Ir (ppm)	Mo (ppm)	Ru (ppm)	Pt (ppm)	Rh (ppm)
Kamacite								
	0.05	0.75	0.61	0.82	6.45	3.99	3.89	1.04
	0.10	0.84	0.74	0.98	7.12	4.64	4.22	1.08
	0.06	0.97	0.70	0.94	6.02	3.93	3.79	0.92
Average	0.07	0.85	0.68	0.91	6.53	4.19	3.97	1.02
SD	0.03	0.11	0.07	0.09	0.55	0.40	0.23	0.08
CI-norm average	1.75	1.68	7.59	1.90	7.02	6.16	4.05	7.25
Taenite								
	0.10	1.47	0.77	1.26	10.49	10.49	6.29	1.68
	0.10	1.47	0.84	1.47	8.30	10.50	7.46	1.47
	0.07	0.99	0.76	0.89	10.61	13.26	5.86	1.77
Average	0.09	1.31	0.79	1.21	9.80	11.42	6.53	1.64
SD	0.02	0.27	0.04	0.29	1.30	1.60	0.83	0.15
CI-norm average	2.28	2.57	8.77	2.52	10.53	16.79	6.67	11.71

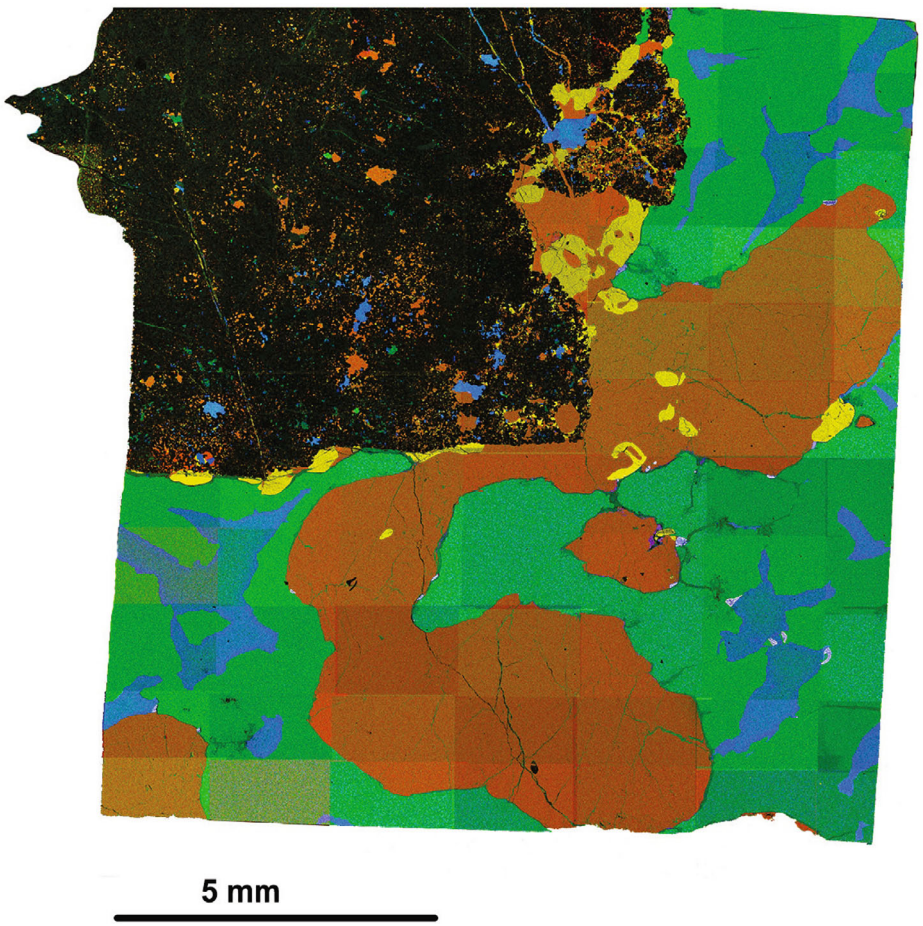

FIGURE 6. Multi-element x-ray map showing the distribution of Fe (green), Ni (blue), P (yellow), and S (red) in RKP Chaunskij. (a) Kamacite (green), taenite (blue), schreibersite (white/lilac), phosphate (yellow), troilite (orange) are present in this sample. Chaunskij consists of metal clasts containing one large silicate clast and a large sinuous grain of troilite (orange). Phosphates are larger in size than schreibersite and are mostly associated with the outer edge of the large silicate clast. Small schreibersite grains occur along the edges of taenite and troilite in the metal clast.

Co (ppm)	Ni (wt%)	Fe (wt%)	Pd (ppm)	Au (ppm)	Cu (ppm)	P (ppm)	Ga (ppm)	Ge (ppm)
5242.17	7.04	92.44	2.44	0.85	55.85	641.24	9.36	40.33
5529.69	7.09	92.35	2.92	0.83	55.49	633.61	8.66	44.43
5287.98	7.34	92.13	3.05	1.07	62.36	654.09	8.85	43.46
5353.28	7.16	92.31	2.80	0.92	57.90	642.98	8.96	42.74
154.48	0.16	0.16	0.32	0.13	3.86	10.35	0.36	2.14
10.58	6.65	5.01	5.01	6.13	0.44	0.69	0.92	1.31
1387.78	36.40	63.46	17.83	3.99	989.17	64.20	39.86	79.72
1429.08	41.27	58.59	24.15	6.93	1308.33	98.49	64.05	97.65
1217.54	41.76	58.11	19.89	4.42	1057.34	49.83	48.61	92.81
1344.80	39.81	60.06	20.62	5.11	1118.28	70.84	50.84	90.06
112.13	2.96	2.96	3.22	1.59	168.08	25.00	12.25	9.28
2.66	36.96	3.26	36.83	34.08	8.54	0.08	5.24	2.76

DISCUSSION

Although the major impetus for this research was understanding redox reactions during metal–silicate mixing, our data can be used to examine all three stages of mesosiderite formation. Here, we address each stage from the earliest to most recent from the perspective of metal textures, metallography, mineralogy, and major, minor, and trace element composition. We then apply the interpretation of our data in the context of a coherent formational model for the mesosiderites.

Initial Crystallization

The metal clasts within the mesosiderites studied here exhibit similar concentrations of many of the moderately and volatile siderophile elements, including Co, Ni, Fe, Pd, Au, and Cu (Tables 2, 4, 5; Figure 7). In contrast, the highly siderophile elements (HSE, Re, Os, Ir, Ru, Pt, Rh) differ. The consensus in the mesosiderite literature is that the restricted range in Ir concentrations in mesosiderites suggests the metal was molten at the time of mixing and that fractional crystallization did not occur (Hassanzadeh et al., 1990; Wasson et al., 1974, 1998). The low Ir concentrations in Chaunskij and RKP A70015 have been previously classified as anomalous (Hassanzadeh et al., 1990; Wasson et al., 1974, 1998). However, although limited to only five samples, the range in HSE reported here is reminiscent of the range observed in IIIAB irons (Figure 7c). In the IIIAB irons, the HSE (Re, Os, Ir, Ru, Pt, Rh) exhibit orders of magnitude variation owing to their strong preference for the solid metal phase compared to the liquid metal. For example, IIIAB iron Ir concentrations show three orders of magnitude variation (Wasson, 1999; Wasson et al., 1998), while the mesosiderites studied here show approximately two orders (Figure 7). Class A/B mesosiderites have the highest Ir concentrations, Chaunskij the lowest, and class C (RKP A79015) is intermediate (Tables 2, 4, and 5; Figure 7a,b). In contrast to the HSE, W and Mo show a much smaller range between the mesosiderites in this study. This is consistent with these elements exhibiting less affinity for the crystallizing metal, as reflected by their partition coefficients (Chabot et al., 2017), and is suggestive of fractional crystallization.

Partition coefficients, in fact, perhaps give the most convincing argument for the differences in the HSE observed here representing a fractional crystallization trend and not the formation of the anomalous mesosiderites on a separate parent body (or bodies), as has been previously argued (e.g., Dhaliwal et al., 2021; Hassanzadeh et al., 1990). The concentration of elements with partition coefficients close to or around 1 (Co, Pd, Ni, Au) is strikingly similar between all the mesosiderites in this study; whereas those elements with partition coefficients that are primarily controlled by the composition (e.g., P and S content) of the liquid metal (Re, Os, Ir, Pt) differ considerably (Figure 7a,b; Chabot et al., 2017; Cook et al., 2004; Petaev & Jacobsen, 2004; and references therein). A separate parent body model would require three parent bodies for mesosiderite metals, with almost identical Co, Pd, Ni, and Au contents, but dramatically different Re, Os, Ir, and Pt to undergo the core disruption, metal–silicate mixing, and slow cooling required to form the mesosiderites. We propose that it is more likely that the differences observed between the HSEs (Figure 7) are a result of a fractional crystallization.

However, the entire metallic mass sampled by mesosiderites did not undergo fractional crystallization, as that should have produced a range of Ir concentrations across all mesosiderites, which is not observed; the vast majority of mesosiderites exhibit a

TABLE 5. Siderophile element abundances for Chaunskij metal clast collected by LA-ICP-MS.

	Re (ppm)	Os (ppm)	W (ppm)	Ir (ppm)	Mo (ppm)	Ru (ppm)	Pt (ppm)	Rh (ppm)
Kamacite	0.01	0.07	0.17	0.07	5.03	0.71	0.50	0.42
	0.01	0.14	0.21	0.20	3.52	1.85	0.76	0.53
	0.01	0.20	0.13	0.19	4.82	1.57	0.71	0.44
	0.01	0.20	0.25	0.21	4.68	1.56	0.69	0.48
	0.02	0.14	0.14	0.19	5.28	1.60	0.74	0.48
Average	0.01	0.15	0.18	0.17	4.67	1.46	0.68	0.47
SD	0.01	0.05	0.05	0.06	0.68	0.44	0.10	0.04
CI-norm average	0.28	0.30	2.01	0.36	5.02	2.15	0.70	3.35
Taenite	0.00	0.15	0.31	0.10	7.57	2.99	0.78	0.76
	-	0.14	0.27	0.09	7.23	2.77	0.75	0.78
	0.03	0.39	0.25	0.18	7.38	1.96	1.02	0.83
	0.02	0.20	0.32	0.20	6.46	2.71	0.70	0.82
	0.01	0.42	0.22	0.32	6.81	2.61	0.84	0.83
Average	0.02	0.26	0.27	0.18	7.09	2.61	0.82	0.81
SD	0.01	0.14	0.04	0.09	0.45	0.39	0.12	0.03
CI-norm average	0.39	0.51	3.05	0.37	7.62	3.83	0.83	5.75

similar and restricted range of the HSE. Fractional crystallization of mesosiderite metal was suggested previously by Kong et al. (2008) to explain the compositional differences between matrix and clast metal in the mesosiderite Dong Ujimqin Qi. In this work, comparing matrix kamacite to clast kamacite, we do not observe a compositional difference between these two populations that can be attributed to this process (Tables 2 and 3; Figure 2).

Matrix Metal–Silicate Mixing

Mixing metal and silicate material in mesosiderites had a profound influence on their textures, chemistry, and mineralogy. It is widely accepted that redox reactions occurred between the metal and silicates based on the Fe-Mg-Mn systematics of the silicates, which are consistent with reduction of FeO in the silicates to native iron and oxidation of P in the metal to produce the abundant phosphates observed in mesosiderites (e.g., Figures 1, 5, 6; Agosto, 1985; Fuchs, 1969; Harlow et al., 1982; Mittlefehldt, 1990; Mittlefehldt et al., 1979; Nehru et al., 1978; Powell, 1971). The phosphates in the mesosiderites studied here are primarily associated with the silicates and matrix metal and not the clast metal (Figures 1, 5, 6), which supports a redox model for matrix metal formation as they record these reactions. Compositional comparisons, therefore, between the two metal populations should highlight differences resulting from such reactions.

Elements of similar volatility should have similar abundances in the matrix and clasts in the absence of redox reactions. In contrast to metal clasts, matrix metal is depleted in P relative to the other volatile siderophiles (e.g., Ga; Tables 2 and 3; Figure 2). The higher kamacite/taenite ratio in the matrix compared to the metal clasts can be explained by the production of excess Fe by the reduction of FeO from the silicates (Figures 1, 5, and 6). Harlow et al. (1982) calculated that the proposed redox reactions would take place at temperatures between 970 and 1030°C. While the solidus for Fe-Ni alloys is significantly higher than these temperatures (Goldstein, 1973), the presence of P is known to suppress the solidus to significantly lower temperatures (Doan & Goldstein, 1970). Therefore, mesosiderite metal, which contains P, has a predicted solidus of <800°C (Harlow et al., 1982). This lower temperature allows the excess metallic Fe produced by redox reactions involving the silicates to raise the matrix metal Fe/Ni value before kamacite exsolution. Consequently, this produced the increased kamacite/taenite ratio of the matrix metal compared to the isolated metal clasts.

The composition and mineralogy of the metal reported here are broadly consistent with, and provide further evidence for, previously proposed redox reactions. However, other readily oxidizable elements within the matrix metal appear unaffected by redox. Mo and Cu are depleted relative to elements of similar volatility in the matrix metal versus the metal clasts (Table 3; Figure 2). For example, the CI-normalized Mo/Ir ratio of matrix metal in Crab Orchard is 0.48 compared to a value of 0.79 for the clast metal, and that for Cu/Au is 0.07 in the matrix and 0.28 in the clast (Table 3). If these depletions are also related to redox and we assume ideal behavior, the T-fO_2 buffer curves should indicate that these elements are more readily oxidized than those elements that do not show any depletions, such as W. The buffer curve for Mo-MoO_2 is ~1 log unit above iron–wüstite (Righter et al., 2017). W-WO_2 lies slightly below iron–wüstite (O'Neill & Pownceby, 1993; Righter et al., 2017). Thus, if Mo is being oxidized, then

Co (ppm)	Ni (wt%)	Fe (wt%)	Pd (ppm)	Au (ppm)	Cu (ppm)	P (ppm)	Ga (ppm)	Ge (ppm)
6055.16	6.32	93.08	2.24	0.63	48.45	175.16	3.17	13.04
6283.26	6.31	93.06	2.69	0.67	54.70	232.71	3.80	16.69
6173.19	6.66	92.73	2.75	0.70	57.03	233.04	4.23	15.73
6382.32	6.83	92.53	2.83	0.63	72.15	264.22	4.78	17.55
6371.06	6.46	92.90	2.64	0.71	57.47	108.35	4.81	16.02
6253.00	6.52	92.86	2.63	0.67	57.96	202.70	4.16	15.81
138.82	0.23	0.23	0.23	0.03	8.71	61.78	0.69	1.70
12.36	6.05	5.04	4.69	4.45	0.44	0.22	0.43	0.48
1732.52	32.38	67.45	14.94	2.69	919.56	52.80	16.94	27.90
1902.13	30.79	69.02	14.85	2.77	820.86	35.65	14.85	26.73
2098.48	32.19	67.60	16.15	2.88	869.85	53.07	17.30	27.69
2414.82	28.84	70.91	13.54	1.98	711.22	63.52	12.50	22.91
1950.69	30.10	69.70	15.13	2.52	855.11	44.56	16.82	28.59
2019.73	30.86	68.94	14.92	2.57	835.32	49.92	15.68	26.76
256.60	1.48	1.46	0.93	0.36	77.93	10.44	2.02	2.25
3.99	28.65	3.74	26.65	17.13	6.38	0.05	1.61	0.82

these same reactions should also produce a corresponding depletion in W as it is oxidized more readily than Mo. No such depletion is observed, with a CI-normalized W/Ir ratio of 0.97 (Table 3). Oxidation of Cu would require considerably more oxidizing conditions, as the Cu-Cu_2O approximates hematite–magnetite (O'Neill & Pownceby, 1993), which is supported by the presence of metallic Cu and absence of copper oxides in meteoritic materials. Phosphorous oxidizes at lower fO_2 conditions than Mo and Cu (Friel & Goldstein, 1976; Olsen & Fuchs, 1967).

The relatively oxidizing conditions required for oxidation of Mo and Cu suggest that additional processes operated during the formation of mesosiderites to explain the composition of the matrix metal. One possible process for Cu is the exsolution or crystallization of metallic Cu, as observed in the Newport pallasite (Buseck, 1968). Ramdohr (1965) observed metallic copper in the Patwar type A mesosiderite. However, our petrographic analysis and multispectral elemental mapping of mesosiderites in this study did not reveal the presence of metallic Cu. Our data show that Cu is correlated with Ni throughout all samples. This suggests that this Cu depletion could be a result of Cu-partitioning between kamacite and taenite, as observed by Kong et al. (1998) in metal nodules within ordinary chondrites. This could also explain the slight depletions in Pd and Au, as they have a strong preference for taenite over kamacite (Hirata & Nesbitt, 1997; Rasmussen et al., 1988).

Similar partitioning-related depletions between kamacite and taenite have not been observed in the literature for Mo. Our analyses show taenite is enriched in Mo relative to kamacite (Figure 4), but the data overlap at the 1σ level. Therefore, another process must have occurred to produce the Mo depletions observed in the matrix metal. An alternative explanation for the data is that sulfurization may have played a role in sequestering it from the metallic phase as Mo is known to exhibit slight chalcophile behavior (Barnes, 2018). However, investigating the role of sulfidization on Mo-contents in mesosiderite metal would require extensive measurement of co-existing sulfides, which is outside the scope of this study.

Slow Cooling

Subgroup 1 mesosiderites contain pigeonite that has not inverted to orthopyroxene (Floran, 1978; Powell, 1971). In contrast, metal clasts commonly contain exsolved kamacite and taenite, reflective of the faster diffusion rates in metallic alloys compared to silicates (Chakraborty, 2008; Ganguly, 2002). The slow cooling of mesosiderites is a well-established—and enigmatic—feature of these meteorites (Bogard et al., 1990; Haack et al., 1996; Hopfe & Goldstein, 2001; Powell, 1969). The mesosiderites studied here show slow cooling effects in both exsolution textures in the metal clasts and homogeneity of taenite (Table 1; Figures 1, 5, and 6). This apparent disconnect between indicators of slow cooling in silicates and those in metal suggests that subgroup 1 mesosiderites could be further subdivided based on indicators of thermal history within the metal.

Mesosiderite Formation Models

The three-stage formation of mesosiderites is hard to explain, particularly the paucity of mantle material and the slow cooling rate after crustal material is mixed with the molten metal. The HSE within the metal of RKP A79105 and Chaunskij show evidence

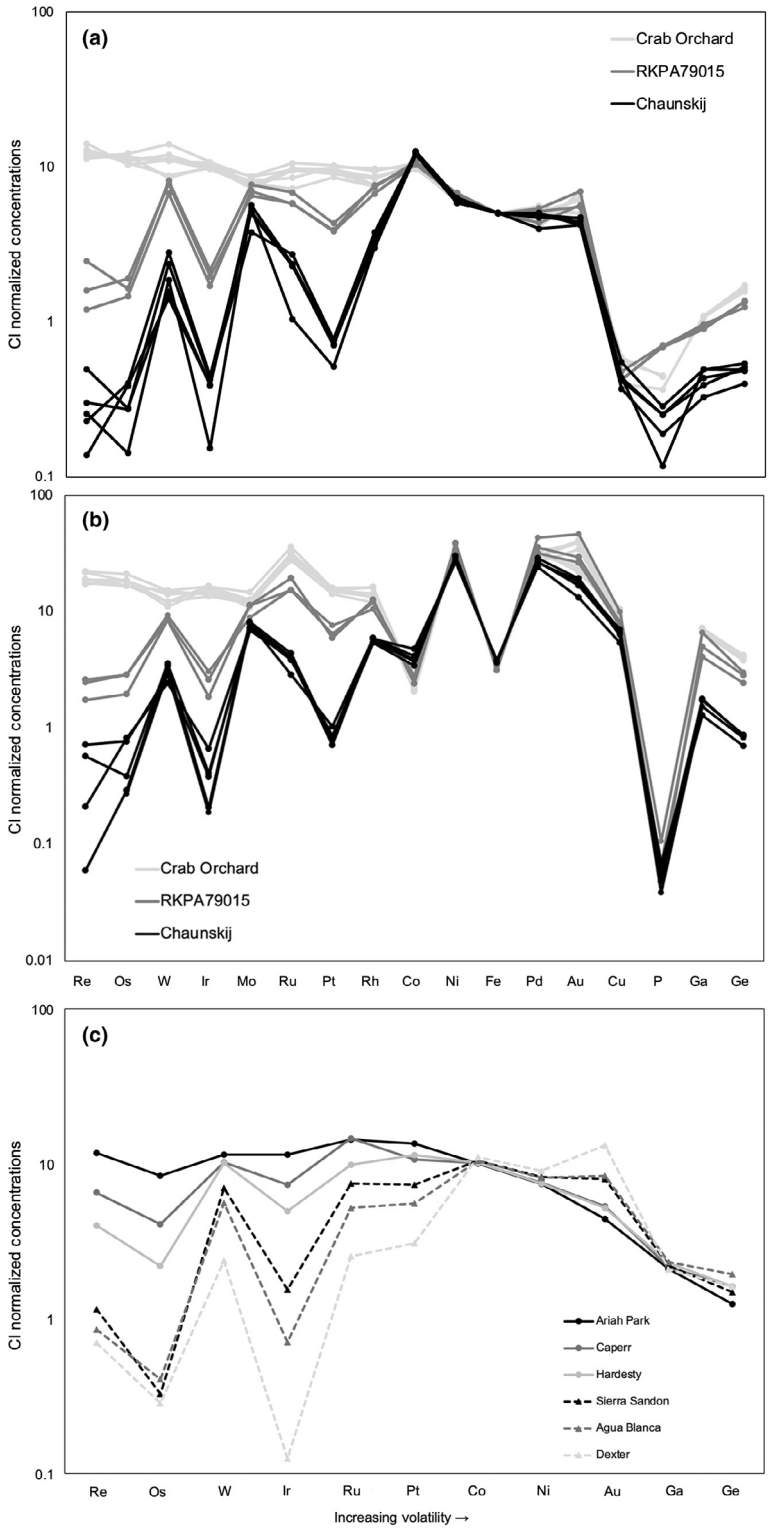

FIGURE 7. Metal clast compositions of class A/B and anomalous mesosiderites in (a) kamacite and (b) taenite compared to (c) IIIAB iron meteorite bulk compositions from Chabot & Zhang, 2022; Table 1). Class A and B mesosiderite metal clasts show high concentrations of highly siderophile elements, Chaunskij shows low concentrations of highly siderophile elements, and RKP A79015 shows concentrations of highly siderophile elements that lie between classes A and B and Chaunskij. This trend is suggestive of fractional crystallization and matches the trend observed for the IIIAB irons. [Correction added on 07 Sep 2023, after first online publication: Figure 7 was updated.]

for fractional crystallization. This has been noted before for RKP A79015 (Dhaliwal et al., 2021; Hazzanzadeh et al., 1990), but these studies invoke its formation on a separate parent body. However, the progressive fractional crystallization trend we observe in the data presented here and its similarity to patterns seen in other fractionally crystallized iron meteorites (Wasson, 1999; Wasson et al., 1998; Worsham et al., 2016) suggest that all mesosiderites originated on the same parent body by the same process. Therefore, any model for their formation must be able to explain how a small number of the mesosiderites sampled a partially differentiated metallic portion of the same parent body as the rest of the group. One possibility is that the metal within RKP A79015 and Chaunskij is the crystallized outer surface of the predominantly molten metallic mass that mixed with the mesosiderite silicates. This scenario is unlikely as that early crystallizing material would be expected to have higher siderophile element concentrations (e.g., Ir), while these meteorites have lower concentrations. Instead, we suggest that localized fractional crystallization occurred in the metallic mass sampled by mesosiderites.

Here, we propose that the impact that produced the molten metallic mass sampled by types A and B mesosiderites produced a smaller mass, with a higher surface to volume ratio and faster cooling, that fractionally crystallized to produce RKP A79015 and Chaunskij. Given the constraint that the metal in types A and B mesosiderites was molten at the time it impacted, it is possible that the event that stripped the silicate shell from this molten metallic core prior to the mesosiderite mixing event occurred both temporally and proximally close to the differentiated asteroid from which the crustal silicates were derived. Hit-and-run collisions can result in the separation and loss of silicate crust and mantle from their corresponding metallic core (Asphaug et al., 2006; Scott et al., 2015); it is possible that only the core material reaccreted onto the parent asteroid and mixed with the crust to form mesosiderites. Additionally, the production of multiple masses of a range of sizes, which in this case would be molten metal, is a natural consequence of hit-and-run collisions (Asphaug et al., 2006; Scott et al., 2015), perhaps providing a mechanism for producing compositionally related bodies that differed in their extent of crystallization. This geochemical model can account for the formation of all mesosiderites on one parent body, but it does not address the plausibility of the physical requirements necessary to explain the slow cooling rates of the molten metal after mixing with the silicate crust. However, two recent studies by Haba et al. (2019) and Sugiura et al. (2022) present physical models for mesosiderite formation on Vesta that can be used to assess this.

Sugiura et al. (2022) propose the mixing of the crust and metal core of the same parent body as a likely mechanism for mesosiderite formation. They model a giant impact on two structurally different differentiated Vesta-like asteroids, one with a thin crust (40 km) with core of 110 km and the other a thick crust (80 km) and larger metal core (140 km). A possible genetic relationship between the mesosiderites and the HEDs has long been recognized, due to similarities between their mineralogy, textures, and bulk compositions (Floran, 1978; Mittlefehldt et al., 1998; Powell, 1971; Rubin & Jerde, 1987; Rubin & Mittlefehldt, 1992), isotopic compositions (Greenwood et al., 2006, 2015; Trinquier et al., 2007, 2008), and ages (Haba et al., 2019). In the latter model (thick crust), even when areas of the core are exposed by the giant impact, mantle material is only found at the impact site. This model may be able to produce a relatively equal proportion of crustal and metal material, as is seen in the mesosiderites, at the surface of the impacted body on a microscale (1–100 cm) (Sugiura et al., 2022). However, while this giant impact model may be able to form mesosiderite-like samples at the surface, how these are subsequently cooled at the slow rates observed in mesosiderites is not addressed. In addition, this model does not provide a mechanism to explain the geochemical data presented here, where small fractions of the molten metal core undergo fractional crystallization but the bulk of the material does not.

Haba et al. (2019) invoke a hit-and-run collision between Vesta and a smaller planetesimal (mass ratio of 0.1). The impact on Vesta ejects crust, mantle, and a small amount of core material. The resulting ejecta covers the original crust of Vesta in two main layers: (1) at the surface, the debris from the impactor would dominate; (2) below the surface, a layer where the underlying crust of Vesta is mixed with the hit-and-run debris. They propose the mesosiderites, with their slow-cooling rates, formed at the bottom of the lower layer.

While our data do not address mesosiderite formation on Vesta, the Haba et al. (2019) model indicates that metal–silicate mixing at depth on a large asteroid could occur, with subsequent burial that produces the range of cooling rates seen in the mesosiderites. This indicates that our geochemical model is possible and would allow for mesosiderite formation on one parent asteroid and include those samples previously identified as anomalous due to their differing Ir concentrations.

CONCLUSIONS

- Our data document redox reactions of matrix metal and silicates during metal–silicate mixing of mesosiderites were localized within the matrix metal

and did not involve mixing with the metal clasts. Evidence for these reactions include P depletions in the matrix metal, phosphate formation in the silicates and matrix metal interface, and the high kamacite/taenite ratio in matrix metal.
- Depletions of Mo in the matrix metal cannot be explained by redox or partitioning behavior, suggesting that other processes must have occurred in addition to redox.
- Metal clast compositions of mesosiderites types A/B, C, and anomalous samples appear consistent with fractional crystallization, for HSE where partition coefficients differ significantly from unity. Trends are less clear in other elements, including Au, where partition coefficients are closer to unity and among the volatile siderophiles.
- We posit a geochemical model where all mesosiderites are formed on the same parent body. A hit-and-run collision stripped the crust and mantle of a differentiated asteroid and produced molten metallic masses of varying sizes from its core. The metal in RKP A79015 and Chaunskij experienced localized fractional crystallization as it was sourced from one of the smaller metallic masses produced by the collision. The molten material collided with the crust of a nearby asteroid and the resulting material was then buried at depth, producing the slow-cooling rates measured for the mesosiderites.

Acknowledgments—We would like to thank D. W. Mittlefehldt, M. K. Haba, and M. K. Weisberg for their discerning comments and reviews, which significantly improved the quality of this manuscript. We are grateful to the Smithsonian Institution Department of Mineral Sciences for the loan of the sections analyzed within this manuscript.

Data Availability Statement—The data that supports the findings of this study are available in the supplementary material of this article.

Editorial Handling—Dr. A. J. Timothy Jull

REFERENCES

Agosto, W. N. 1985. Liquidus Phosphorus Redox Reactions in Mesosiderite Silicates 16th Lunar and Planetary Science Conference, pp. 7–8.

Asphaug, E., Agnor, C. B., and Williams, Q. 2006. Hit-and-Run Planetary Collisions. *Nature* 439: 155–60.

Barnes, S. 2018. Chalcophile Elements. In *Encyclopedia of Geochemistry: A Comprehensive Reference Source on the Chemistry of the Earth*, edited by W. M. White, 229–33. Cham: Springer International Publishing.

Bogard, D. D., and Garrison, D. H. 1998. ^{39}Ar-^{40}Ar Ages and Thermal History of Mesosiderites. *Geochimica et Cosmochimica Acta* 62: 1459–68. https://doi.org/10.1016/s0016-7037(98)00077-5.

Bogard, D. D., Garrison, D. H., Jordan, A. L., and Mittlefehldt, D. 1990. ^{39}Ar-^{40}Ar Dating of Mesosiderites: Evidence for Major Parent Body Disruption <4 Ga Ago. *Geochimica et Cosmochimica Acta* 54: 2549–64.

Buseck, P. R. 1968. Mackinawite, Pentlandite, and Native Copper from the Newport Pallasite. *Mineralogical Magazine and Journal of the Mineralogical Society* 36: 717–25.

Chabot, N. L., Wollack, E. A., McDonough, W. F., Ash, R. D., and Saslow, S. A. 2017. Experimental Determination of Partitioning in the Fe-Ni System for Applications to Modeling Meteoritic Metals. *Meteoritics & Planetary Science* 52: 1133–45.

Chabot, N. L., and Zhang, B. 2022. A Revised Trapped Melt Model for Iron Meteorites Applied to the IIIAB Group. *Meteoritics & Planetary Science* 57: 200–27.

Chakraborty, S. 2008. Diffusion in Solid Silicates: A Tool to Track Timescales of Processes Comes of Age. *Annual Review of Earth and Planetary Sciences* 36: 153–90.

Cook, D. L., Walker, R. J., Horan, M. F., Wasson, J. T., and Morgan, J. W. 2004. Pt-Re-Os Systematics of Group IIAB and IIIAB Iron Meteorites. *Geochimica et Cosmochimica Acta* 68: 1413–31.

Delaney, J. S., Nehru, C. E., Prinz, M., and Harlow, G. E. 1982. Metamorphism in Mesosiderites 12th Lunar and Planetary Science Conference, pp. 1315–42.

Dhaliwal, J. K., Horan, M. F., Ash, R. D., Bullock, E. S., and Carlson, R. W. 2021. Insights from Siderophile Elements into the Impact Origin of Mesosiderites 52nd Lunar and Planetary Science Conference, abstract #2236.

Doan, A. S., and Goldstein, J. I. 1970. The Ternary Phase Diagram, Fe-Ni-P. *Metallurgical Transactions* 1: 1759–67.

Floran, R. J. 1978. Silicate Petrography, Classification, and Origin of the Mesosiderites: Review and New Observations 9th Lunar and Planetary Science Conference, pp. 1053–81.

Friel, J. J., and Goldstein, J. I. 1976. An Experimental Study of Phosphate Reduction and Phosphorus-Bearing Lunar Metal Particles. 7th Lunar and Planetary Science Conference, pp. 791–806.

Fuchs, L. H. 1969. The Phosphate Mineralogy of Meteorites. *Astrophysics and Space Science Library*: 683–95. https://doi.org/10.1007/978-94-010-3411-1_56.

Ganguly, J. 2002. Diffusion Kinetics in Minerals: Principles and Applications to Tectono-Metamorphic Processes. *EMU Notes in Mineralogy* 4: 271–309.

Goldstein, J. I. 1973. Fe-Ni Phase Diagram. In *Metals Handbook, Vol. 8*, edited by T. Lyman, 8th ed., 304. Ohio: American Society for Metals, Metals Park.

Greenwood, R. C., Barrat, J., Scott, E. R. D., Haack, H., Buchanan, P. C., Franchi, I. A., Yamaguchi, A., Johnson, D., Bevan, A. W. R., and Burbine, T. H. 2015. Geochemistry and Oxygen Isotope Composition of Main-Group Pallasites and Olivine-Rich Clasts in Mesosiderites: Implications for the "Great Dunite Shortage" and HED-Mesosiderite Connection. *Geochimica et Cosmochimica Acta* 169: 115–36.

Greenwood, R. C., Franchi, I. A., Jambon, A., Barrat, J. A., and Burbine, T. H. 2006. Oxygen Isotope Variation in Stony-Iron Meteorites. *Science* 313: 1763–5.

Haack, H., Scott, E. R. D., and Rasmussen, K. L. 1996. Thermal and Shock History of Mesosiderites and their Large Parent Asteroid. *Geochimica et Cosmochimica Acta* 60: 2609–19.

Haba, M. K., Wotzlaw, J., Lai, Y., Yamaguchi, A., and Schönbächler, M. 2019. Mesosiderite Formation on Asteroid 4 Vesta by a Hit-and-Run Collision. *Nature Geoscience* 12: 510–5.

Harlow, G. E., Delaney, J. S., Nehru, C. E., and Prinz, M. 1982. Metamorphic Reactions in Mesosiderites: Origin of Abundant Phosphate and Silica. *Geochimica et Cosmochimica Acta* 46: 339–48.

Hassanzadeh, J., Rubin, A. E., and Wasson, J. T. 1990. Compositions of Large Metal Nodules in Mesosiderites: Links to Iron Meteorite Group IIIAB and the Origin of Mesosiderite Subgroups. *Geochimica et Cosmochimica Acta* 54: 3197–208. https://doi.org/10.1016/0016-7037(90)90134-7.

Hewins, R. H. 1984. The Case for a Melt Matrix in Plagioclase-POIK Mesosiderites. *Journal of Geophysical Research: Solid Earth* 89: C289–97.

Hewins, R. H. 1988. Petrology and Pairing of Mesosiderites from Victoria Land, Antarctica. *Meteoritics* 23: 123–9.

Hirata, T., and Nesbitt, R. W. 1997. Distribution of Platinum Group Elements and Rhenium Between Metallic Phases of Iron Meteorites. *Earth and Planetary Science Letters* 147: 11–24.

Hopfe, W. D., and Goldstein, J. I. 2001. The Metallographic Cooling Rate Method Revised: Application to Iron Meteorites and Mesosiderites. *Meteoritics & Planetary Science* 36: 135–54.

Keil, K., Stöffler, D., Love, S. G., and Scott, E. R. D. 1997. Constraints on the Role of Impact Heating and Melting in Asteroids. *Meteoritics & Planetary Science* 32: 349–63.

Kong, P., Ebihara, M., and Xie, X. 1998. Reevaluation of Formation of Metal Nodules in Ordinary Chondrites. *Meteoritics & Planetary Science* 33: 993–8. https://doi.org/10.1111/j.1945-5100.1998.tb01706.x.

Kong, P., Su, W., Li, X., Spettel, B., Palme, H., and Tao, K. 2008. Geochemistry and Origin of Metal, Olivine Clasts, and Matrix in the Dong Ujimqin Qi Mesosiderite. *Meteoritics & Planetary Science* 43: 451–60.

Krot, A. N., Keil, K., Scott, E. R. D., Goodrich, C. A., and Weisberg, M. K. 2014. 1.1—Classification of Meteorites and their Genetic Relationships. In *Treatise on Geochemistry*, edited by H. D. Holland, and K. K. Turekian, 2nd ed., 1–63. Oxford: Elsevier.

Mittlefehldt, D. W. 1990. Petrogenesis of Mesosiderites: I. Origin of Mafic Lithologies and Comparison with Basaltic Achondrites. *Geochimica et Cosmochimica Acta* 54: 1165–73.

Mittlefehldt, D. W., Chou, C., and Wasson, J. T. 1979. Mesosiderites and Howardites: Igneous Formation and Possible Genetic Relationships. *Geochimica et Cosmochimica Acta* 43: 673–88.

Mittlefehldt, D. W., McCoy, T. J., Goodrich, C. A., and Kracher, A. 1998. Non-Chondritic Meteorites from Asteroidal Bodies. *Reviews in Mineralogy and Geochemistry* 36: 4.1–4.195.

Nehru, C. E., Harlow, G. E., Prinz, M., and Hewins, R. H. 1978. The Tridymite-Phosphate-Rich Component in Mesosiderites. *Meteoritics* 13: 573.

Nininger, H. H. 1963. Meteorite with Unique Features. *Science* 139: 345–7.

Olsen, E., and Fuchs, L. H. 1967. The State of Oxidation of some Iron Meteorites. *Icarus* 6: 242–53.

O'Neill, H. S. C., and Pownceby, M. I. 1993. Thermodynamic Data from Redox Reactions at High Temperatures. I. An Experimental and Theoretical Assessment of the Electrochemical Method Using Stabilized Zirconia Electrolytes, with Revised Values for the Fe-"FeO", Co-CoO, Ni-NiO and Cu-Cu_2O Oxygen Buffers, and New Data for the W-WO_2 Buffer. *Contributions to Mineralogy and Petrology* 114: 296–314.

Petaev, M. I., Clarke, R. S., Jr., Olsen, E. J., Jarosewich, E., Davis, A. M., Steele, I. M., Lipschutz, M. E., et al. 1993. Chaunskij: The Most Highly Metamorphosed, Shock-Modified and Metal-Rich Mesosiderite, pp. 1131.

Petaev, M. I., and Jacobsen, S. B. 2004. Differentiation of Metal-Rich Meteoritic Parent Bodies: I. Measurements of PGEs, Re, Mo, W, and Au in Meteoritic Fe-Ni Metal. *Meteoritics & Planetary Science* 39: 1685–97. https://doi.org/10.1111/j.1945-5100.2004.tb00066.x.

Powell, B. N. 1969. Petrology and Chemistry of Mesosiderites —I. Textures and Composition of Nickel-Iron. *Geochimica et Cosmochimica Acta* 33: 789–790. https://doi.org/10.1016/0016-7037(69)90027-1.

Powell, B. N. 1971. Petrology and Chemistry of Mesosiderites—II. Silicate Textures and Compositions and Metal-Silicate Relationships. *Geochimica et Cosmochimica Acta* 35: 5–34.

Ramdohr, P. 1965. Über Mineralbestand von Pallasiten und Mesosideriten und Einige Genetische Überlegungen. *Monatsberichte der Deutschen Akademie der Wissenschaftten zu Berlin* 7: 923–38.

Rasmussen, K. L., Malvin, D. J., and Wasson, J. T. 1988. Trace Element Partitioning Between Taenite and Kamacite: Relationship to the Cooling Rates of Iron Meteorites. *Meteoritics* 23: 107–12. https://doi.org/10.1111/j.1945-5100.1988.tb00905.x.

Righter, K., Pando, K., Ross, D. K., Butterworth, A. L., Gainsforth, Z., Jilly-Rehak, C. E., and Westphal, A. J. 2017. Oxygen Buffering in High Pressure Solid Media Assemblies: New Approach Enabling Study of fO_2 from IW-4 to IW+4.5.

Rubin, A. E., and Jerde, E. A. 1987. Diverse Eucritic Pebbles in the Vaca Muerta Mesosiderite. *Earth and Planetary Science Letters* 84: 1–14.

Rubin, A. E., Kallemeyn, G. W., Wasson, J. T., Clayton, R. N., Mayeda, T. K., Grady, M., Verchovsky, A. B., Eugster, O., and Lorenzetti, S. 2003. Formation of Metal and Silicate Globules in Gujba: A New Bencubbin-Like Meteorite Fall. *Geochimica et Cosmochimica Acta* 67: 3283–98.

Rubin, A. E., and Mittlefehldt, D. W. 1992. Classification of Mafic Clasts from Mesosiderites: Implications for Endogenous Igneous Processes. *Geochimica et Cosmochimica Acta* 56: 827–40.

Scott, E. R. D., Haack, H., and Love, S. G. 2001. Formation of Mesosiderites by Fragmentation and Reaccretion of a Large Differentiated Asteroid. *Meteoritics & Planetary Science* 36: 869–91.

Scott, E. R. D., Keil, K., Goldstein, J. I., Asphaug, E., Bottke, W. F., and Moskovitz, N. A. 2015. Early Impact History and Dynamical Origin of Differentiated Meteorites and Asteroids. *Asteroids IV*. https://doi.org/10.2458/azu_uapress_9780816532131-ch030.

Sugiura, K., Haba, M. K., and Genda, H. 2022. Giant Impact onto a Vesta-Like Asteroid and Formation of

Mesosiderites through Mixing of Metallic Core and Surface Crust. *Icarus* 379: 114949.
Trinquier, A., Birck, J., and Allegre, C. J. 2007. Widespread ^{54}Cr Heterogeneity in the Inner Solar System. *The Astrophysical Journal* 655: 1179–85. https://doi.org/10.1086/510360.
Trinquier, A., Birck, J.-L., Allègre, C. J., Göpel, C., and Ulfbeck, D. 2008. ^{53}Mn–^{53}Cr Systematics of the Early Solar System Revisited. *Geochimica et Cosmochimica Acta* 72: 5146–63. https://doi.org/10.1016/j.gca.2008.03.023.
Walker, R. J., McDonough, W. F., Honesto, J., Chabot, N. L., McCoy, T. J., Ash, R. D., and Bellucci, J. J. 2008. Modeling Fractional Crystallization of Group IVB Iron Meteorites. *Geochimica et Cosmochimica Acta* 72: 2198–216.
Wasson, J. T. 1999. Trapped Melt in IIIAB Irons: Solid/Liquid Elemental Partitioning During the Fractionation of the IIIAB Magma. *Geochimica et Cosmochimica Acta* 63: 2875–89. https://doi.org/10.1016/s0016-7037(99)00283-5.
Wasson, J. T., Choi, B., Jerde, E. A., and Ulff-Møller, F. 1998. Chemical Classification of Iron Meteorites: XII. New Members of the Magmatic Groups. *Geochimica et Cosmochimica Acta* 62: 715–24.
Wasson, J. T., and Rubin, A. E. 1985. Formation of Mesosiderites by Low-Velocity Impacts as a Natural Consequence of Planet Formation. *Nature* 318: 168–70.
Wasson, J. T., Schaudy, R., Bild, R. W., and Chou, C. 1974. Mesosiderites—I. Compositions of their Metallic Portions and Possible Relationship to Other Metal-Rich Meteorite Groups. *Geochimica et Cosmochimica Acta* 38: 135–49.
Wilson, W. E., Jr. 1972. The Bondoc Mesosiderite: Mineralogy and Petrology of the Metal Nodules Master's thesis, Arizona State University, Tempe, 74 pp.
Worsham, E. A., Bermingham, K. R., and Walker, R. J. 2016. Siderophile Element Systematics of IAB Complex Iron Meteorites: New Insights into the Formation of an Enigmatic Group. *Geochimica et Cosmochimica Acta* 188: 261–83.

SUPPORTING INFORMATION

Additional supporting information may be found in the online version of this article.

Appendix S1. Supplementary Materials.